This is a preprint, the final version is subject to change, of the American Mineralogist (MSA)
Cite as Authors (Year) Title. American Mineralogist, in press.
DOI: https://doi.org/10.2138/am-2019-7218

Experimental quantification of the Fe-valence state on amosite-asbestos boundaries using acSTEM Dual-Electron Energy-Loss Spectroscopy

[a]Ruggero Vigliaturo, [b]Simone Pollastri, [a,c]Reto Gieré, [d]Alessandro F. Gualtieri, [e]Goran Dražić

[a] *Department of Earth and Environmental Science, University of Pennsylvania, 240 S. 33rd Street, Hayden Hall, Philadelphia, PA 19104-6316, U.S.A.*

[b] *CERIC – ERIC, Strada Statale 14 - km 163.5, 34149 Basovizza, Trieste, Italy*

[c]*Center of Excellence in Environmental Toxicology, University of Pennsylvania, Philadelphia, PA*

[d] *Dipartimento di Scienze Chimiche e Geologiche, Università degli studi di Modena e Reggio Emilia, I-41125, Modena, Italy*

[e]*Department for Materials Chemistry, National Institute of Chemistry, Hajdrihova ulica 19, 1000, Ljubljana, Slovenia*

Abstract

The determination of the oxidation state and the coordination geometry of iron expands the knowledge obtained by standard mineralogical characterization. It provides information that is crucial in assessing the potential of minerals to interact with the surrounding environment and to generate reactive oxygen species, which can disrupt the normal function of living organisms. Aberration-corrected Scanning Transmission Electron Microscopy Dual-Electron Energy-Loss Spectroscopy (acSTEM Dual-EELS) has only rarely been applied in environmental and medical mineralogy, but it can return data that are essential for the description of near-surface and surface

mechanisms involved in many environmental and health-related processes. In this study, we have applied the energy-loss near-edge structure (ELNES) and the $L_{2,3}$ white-line intensity-ratio methods using both the universal curve and progressively larger integrating windows to verify their effectiveness in satisfactorily describing the state of iron in amosite grain boundaries, and, at the same time, to estimate thickness in the same region of interest. The average valence state obtained from acSTEM Dual-EELS and from a simplified geometrical model were in good agreement, and within the range defined by the bulk and the measured surface-valence states. In the specific case presented here, the use of the universal curve was most suitable in defining the valence state of iron in amosite grain boundaries. The study of ELNES revealed an excellent correspondence with the valence state determined by the $L_{2,3}$ white-line intensity-ratio method through the use of the universal curve, and it seems that the spectra carry some information regarding the coordination geometry of Fe. The combination of visual examination, reconstruction of the grain boundaries through a simple geometrical model, and Dual-EELS investigation is a powerful tool for characterizing the grain boundaries of hazardous minerals and foreseeing their potential activity in an organism, with the possibility to describe toxic mechanisms in a stepwise fashion.

Keywords

Dual Electron Energy-Loss Spectroscopy; Fe-valence state; amphibole; asbestos; surface chemistry; spatially resolved crystal-chemistry

Introduction

The valence state of Fe in members of the amphibole supergroup plays an important role when elucidating mineralogical and geological history since it can be influenced by multiple geochemical reactions in a wide range of conditions (Cavé et al., 2006). It can further contribute to the understanding of the redox conditions in which these minerals crystallized (Garvie and Busek, 1998), and of weathering, dissolution and recrystallization processes to which these minerals were exposed in the natural environment. When in contact with living cells, the mixed-valence state of Fe in amphiboles can determine the mineral's potential in disrupting Fe homeostasis and in generating reactive oxygen species (ROS) in cells and at the systemic level (Jablonski et al., 2017). The generation of ROS may lead to several respiratory diseases (e.g., asbestosis, pleural abnormalities) and malignancies, such as squamous cell carcinoma, small-cell and large-cell carcinoma, and adenocarcinoma (Pacella et al., 2012), including mesothelioma, which is strictly related to asbestiform minerals. Amphiboles that are not necessarily classified as asbestos or asbestiform were recently also suggested to be related to autoimmune disease (Li et al., 2012; Ferro et al., 2013; Pfau et al., 2014), which makes the description of the toxicity caused by these minerals even more pressing. During interaction with the biological environment, Fe in asbestiform minerals plays different roles depending on its oxidation state, coordination, and surface-site occupancy (Gualtieri et al., 2016). ROS may be generated when Fe is released into cells or biofluids, or during surface-bound Fe-promoted reactions (Schoonen et al., 2006). Therefore, the possibility to determine both valence and bonding of Fe at an atomic- or nano-scale allows for a detailed description of the mechanisms that can potentially lead to generation of ROS, understanding the transformation of these minerals, and foreseeing the sequence of

events causing related pathology, while bearing in mind that Fe is just one of the variables contributing to these mechanisms.

The determination of Fe-valence state, coordination geometry and local morphometry in a specific observable region of interest (ROI) of a (potentially) hazardous mineral can thus provide a very important contribution to the comprehension of the early mechanisms by which diseases may be triggered.

The use of aberration-corrected scanning transmission electron microscopy (acSTEM) and Dual-Electron Energy-Loss Spectroscopy (Dual-EELS) allows for simultaneous collection of two spectra at different energy-loss ranges in a specific ROI on individual particles. This translates to an immediate alignment of the zero-loss peak and, therefore, side-steps the need to collect two consecutive spectra on the same sample area to perform the alignment (Potapov and Schryvers, 2004), resulting in a shorter exposure of the ROI to the electron beam, thus reducing potential electron-beam damages and operational time. Application of Dual-EELS has a great advantage compared to conventional EELS because it eliminates the need of measuring the low-loss and the high-loss spectra consecutively, allowing for the *in-loco* determination of the ROI thickness simultaneously with its valence state.

The Fe-valence state is commonly determined by techniques with poor spatial resolution, such as Mössbauer spectroscopy and wet chemical analysis, or by indirect stoichiometry-based calculations from electron probe micro-analysis data (e.g., Droop, 1987). Despite the accuracy of redox titration and thermogravimetric approaches in the determination of the oxidation state of an element in a phase, these techniques provide averaged and compound-dependent results (Lee et al., 1980) without satisfactory spatial resolution. Advanced spectroscopic techniques, such as X-Ray Absorption Near-Edge Structure (XANES), Extended X-Ray Absorption Fine Structure

(EXAFS) or Synchrotron Mössbauer Source (SMS) spectroscopy, can provide Fe-valence state data that are accurate and comparable to those obtained from Electron Energy-Loss Near-Edge Structure (ELNES), but again with a far lower spatial resolution. With respect to asbestos-related disease and disease-mechanism studies, X-Ray Photoelectron Spectroscopy (XPS) has been used to track the surface evolution of asbestos fibers in contact with media that simulate biofluids (e.g., Pacella et al., 2015), limiting the investigation to the first ≈10 nm at the surface of the minerals. Even though EELS has a higher spatial resolution than X-Ray Absorption Spectroscopy (XAS) (Taftø and Krivanek, 1982) and related techniques, it has been used in a limited manner in mineralogy, primarily because EELS is commonly intended as a technique mainly dedicated to light elements and complementary to Energy-Dispersive X-ray (EDX) spectroscopy (Andreozzi and Pollastri, 2017). However, EELS can provide additional and more detailed information: acSTEM Dual-EELS is a powerful technique, which allows for simultaneous acquisition of atomic- and nano-scale images and related data on chemical composition, coordination and oxidation state for the exact same area. The technique, therefore, provides invaluable local information on the nature of the observed specimen. Development and application of this technique, thus, give an opportunity to describe surfaces, mineral interfaces, and potentially the atomic-scale sequence of processes within the mineral or at the interface between the mineral and the surrounding chemical environment.

In this study, we systematically apply methods that allow us to determine the Fe-oxidation state from Dual-EELS spectra recorded in several ROIs of naturally occurring amosite, which has been characterized previously (Pollastri et al., 2015). By using acSTEM, we were able to select and orient fiber boundaries to obtain accurate and precise, spatially resolved information. In

addition, we used XPS as an independent technique to assess and discuss the results obtained through acSTEM Dual-EELS on the fibers.

The most common procedure used to determine the valence state of transition metals through EELS is known as the white-line ratio or $L_{2,3}$-ratio method. In this procedure, the formal valence state is correlated with the L_3- and L_2-white lines emerging from the spin-orbit splits that correspond to the $2p_{3/2} \rightarrow 3d$ and $2p_{1/2} \rightarrow 3d$ transitions (Colliex et al., 1991; Riedl et al., 2007). The 3d transition metal white-line intensity ratio has been demonstrated to be different from the expected value of 2 (Leapman and Grunes, 1980). This is a consequence of the interaction between the 3d valence electrons, the ejected electrons, and the core hole. The intensity ratio $I(L_3)/I(L_2)$ assumes maximum values in the $3d^5$ configuration, decreasing toward both the $3d^0$ and $3d^{10}$ configurations (Sparrow et al., 1984; Thole and Van der Laan, 1988). This simply results in a proportional reduction of the white-line intensity ratio while the Fe-valence state approaches its minimum value. The white-line intensity-ratio procedure has several limitations since the $I(L_3)/I(L_2)$ does not necessarily always have a one-to-one correspondence to the Fe-valence state (Sparrow et al., 1984; Graetz et al., 2004; Tan et al., 2012). One of the reported problems is related to the sample thickness, which is described as t/λ, where t is the average thickness of the investigated ROI and λ is the inelastic mean free path of the electrons passing through the analyzed region. The removal of plural-scattering through deconvolution or the investigation of a specific area with $t/\lambda<0.5$ should be satisfactory in limiting the thickness influence on the results (Schmid and Mader, 2006; Varela et al., 2009). While some authors suggest that the $I(L_3)/I(L_2)$ is relatively insensitive to thickness (Wang et al., 2000) below $t/\lambda<0.5$ (Varela et al., 2009), other authors sustain that spectral deconvolution is necessary to obtain an

accurate evaluation of the valence state (Tan et al., 2012). On the other hand, Loomer et al. (2007) reported that there was no thickness effect for t/λ values slightly greater than 1.

In our contribution, the white-line intensity-ratio investigation has been coupled with ELNES in the spectral regions of the O–K and Fe–$L_{2,3}$ edges in an attempt to retrieve information on the Fe-coordination geometry and the contribution of other factors to the relation of spectral shape with the valence state. The applicability of the so-called "universal curve" (Van Aken et al., 1998) was compared to the use of different calibration curves obtained from standards with known valence states. This comparison was made because the investigated ROIs are characterized not only by the complex crystal structure of amphibole but also by the presence of an amorphous shell, which can induce unexpected edge modifications in the ELNES spectra that in turn may affect the extracted valence-state values. In particular, the universal curve uses a narrow window (2eV wide), which can be influenced by both spectral noise and small differences in the ELNES shape (Tan et al., 2012). In view of these possible complications we tested several approaches to assess which $L_{2,3}$ method and integration-window width are most suitable in describing the complexity of the amphibole-fiber boundaries and their modified surfaces.

In addition, we created a simple geometric model to estimate the valence state at particle boundaries starting from Mössbauer spectroscopy and XPS data so that it could be compared with the results obtained through acSTEM Dual-EELS.

The possible influences of thickness and beam damage on the results have been considered.

Materials and methods

Samples of amosite (or asbestiform grunerite) were investigated by two different techniques, XPS and acSTEM Dual-EELS. We need to emphasize that the XPS data were obtained by an independent laboratory (ENEA, Casaccia Research Center, Materials and New Technologies Unit, Rome, Italy), and the data were not made accessible to us until after we had completed our acSTEM Dual-EELS investigation. This approach was chosen to guarantee a non-biased, independent evaluation of our acSTEM Dual-EELS data.

The XPS spectra collected on the bulk fibers, i.e. not separated into short and long fibers, were acquired with a V.G. ESCALAB MKII spectrometer and recorded using an Mg anode (Kα radiation line at 1253.6 eV, non-monochromatized) as X-ray source at a voltage of 10 kV and a power of 240 W. Spectra were collected in the constant-analyzer energy mode at a pass energy of 10 eV and a step channel of 0.1 eV. The sample was suspended in analytical-grade acetone and gently ground in an agate mortar. The powdered material was then transferred onto a double-sided sticky tape on a standard sample holder. To determine the oxidation state of iron, the Fe–$2p_{3/2}$ peak was deconvoluted following the approach described in Fantauzzi et al. (2010).

Two samples of amosite were investigated by acSTEM Dual-EELS, one consisting of short fibers, the other of long fibers. These samples were prepared for this study as described in Pollastri et al. (2014) and from the same batch that was also analyzed by XPS. The two samples were suspended in 2-propanol and then transferred onto separate 300 mesh holey-carbon TEM copper grids (SPI supplies, West Chester, PA, U.S.A.). All experiments were conducted at an operational voltage of 80 kV with an aberration-corrected STEM (JEOL, model ARM 200 F) equipped with a high-brightness Cold-Field Emission Gun (CFEG) and an energy filter (Quantum ER GIF, Gatan, USA) with Dual-EELS capability. The instrument was tuned to a collection semi-angle of 22.65 mrad (8 cm camera length – working distance) to increase the

intensity of the signal on core-loss edges (Colliex et al., 1991) and a convergence semi-angle of 24.00 mrad, using an aperture of 5 mm and a dispersion of 0.25 eV/channel. EELS was performed in dual mode on 100 separate, randomly selected areas of 625 nm^2 each. These areas were located along the grain boundaries of the fibers (50 ROIs each in the short- and long-fiber grids). The first spectral region was recorded over a period of $2 \cdot 10^{-4}$ s, whereas the core-loss region was registered for a duration of 10 s, and in both cases, 3 frames were summed up to generate a spectrum. The recording of 3 consecutive frames allowed us to first screen for the possible "morphological" transformation of ELNES due to beam damage resulting from the exposure of a ROI to the electron beam. The first spectral region ranged from -50 to 462 eV, the core-loss region of the spectra from 500 to 1012 eV, which allowed for simultaneous visualization of the O and Fe edges.

Determination of the ROI thickness

The low-loss region was used to determine the relative sample thickness (t/λ). The relative thickness of each individually analyzed ROI was calculated by determining the ratio between the zero-loss electrons and the total transmitted intensity, according to Poisson's statistics (Malis et al., 1988). All the ROIs with $t/\lambda>0.5$ were arbitrarily discarded from the study.

The real sample thickness was then calculated by estimating the λ value for amosite crystals through the Iakoubovskii et al. (2008) formulation, which is appropriate for a collection semi-angle (β) greater than 20 mrad. The core-loss region was used to study the O- and Fe-ELNES, and to determine the Fe-oxidation state by applying the selected methods. These data, together

198 with literature data, imaging of fiber boundaries, and morphometry were also used to reconstruct
199 the geometry and estimate the expected valence state of the studied amphiboles.

200

201

202 *$L_{2,3}$-ratio method*

203 As a first step, we used an inverse power law to remove the pre-edge background of the collected
204 core-loss EEL spectra (Supplementary S.1). The intensity due to transitions into the continuum
205 was subtracted by applying a double arctangent step function as continuum for the removal of
206 the post-edge background (Supplementary S.1).

207 Three progressively larger integration windows (Supplementary S.2) were tested on spectra
208 obtained on standards using the script "Double Atan EELS Background" created by Mitchell
209 (2015). In the first case, we used two integrating windows (2 eV wide), one located at the
210 maximum of the L_3 edge, and one located at the L_2 edge, as suggested by the modified integral
211 Fe-$L_{2,3}$ white-line intensity method proposed by Van Aken et al. (1998), analogous to the
212 universal curve. In the second case, we applied two integrating windows, which were centered at
213 the peak maxima and which were 4 eV wide (Schmid and Mader, 2006). In the third case, we
214 used two 8 eV wide windows (similar to Tan et al., 2012) with the lower limit of the windows
215 located just after the onset of the L_3 and L_2 edges, respectively (which frequently corresponded
216 to centering the windows on the peak maxima).

217 This procedure was used to determine the correspondence between L_3/L_2 ratios and the valence
218 state in three standards with the known Fe-oxidation states of 2+, 2.7+, and 3+ (Supplementary
219 S.3). The L_3/L_2 ratios versus valence-state data were fitted using an exponential function to

obtain calibration curves. The universal curve (Van Aken et al., 1998) and the equations of the calibration curves were then used to determine the average valence state of ROIs on amphibole fiber boundaries. In this study, the calibration curves were generated using the same standards and the same Atomic Resolution Microscope (ARM) as in Rojac et al. (2017), because the stability of the standards in terms of valence state was already verified on the same instrument.

Results

XPS reference analyses

The XPS analysis, performed on fibers that were not separated into two dimensional categories, revealed a predominance of Fe^{3+} in the forms of Fe^{3+} and of FeOOH (Table 1). From these data, the corresponding average Fe-valence state was calculated at 2.67 with σ_{n-1}=0.04.

ROI thickness, features and geometrical model for amosite

The fibers exhibit straight boundaries, which are in many cases covered by a discontinuous and partially amorphized "shell" of variable thickness (Fig. 1A). This "shell" is very irregular, presenting a rough surface, and exhibits an average thickness of 3.74 nm (σ_{n-1}=2.30) for short fibers and 1.99 nm (σ_{n-1}=0.88) for long fibers. The overall thickness of the investigated ROIs at the fiber boundaries, evaluated from the low-loss spectra, varies between 5.73 and 37.56 nm, with an average value of 20.09 nm (σ_{n-1}=9.68). The average ROI thickness of the short fibers is 16.25 nm (σ_{n-1}=7.69), whereas that of the long fibers is 25.30 nm (σ_{n-1}=9.77). All those areas, where we were not able to orient the crystal or where the thickness t/λ was >0.5 (roughly

corresponding to t>50 nm), were discarded from the subsequent analyses, effectively decreasing the total number of useable areas from 100 to 66 (38 for short fibers, 28 for long fibers).

A geometric model of the ROIs for short and long fibers was created based on the average ROI thickness, average "shell" thickness, and the characteristic cleavage angles of the amphiboles (Fig. 1B).

In our simple geometrical model, we assumed that the features seen in the section perpendicular to the amphibole's *c*-axis remain the same when moving along *c*-axis, namely average oxidation state, "shell" thickness, and morphometry. The section perpendicular to the amphibole's *c*-axis is represented as a trapezoid with acute angles of 62° and obtuse angles of 118°. The ROI width is treated as the height (h) of the trapezoid, whereas the ROI thickness is equivalent to $\frac{B+b}{2}$, where B is the long base and b the short base of the trapezoid. The bases are parallel to the (010) crystallographic plane.

Furthermore, if we assume – as a simplification – that the external shell is completely oxidized and the bulk material is completely reduced, the calculation of the ratio between the perpendicular-section area of the "shell" (A_{shell}: red in Fig. 1B) and the total perpendicular section area (A_{tot}: red plus green in Fig. 1B), yields a rough estimate of the expected average valence state, i.e., $valence\ state = \frac{A_{shell}}{A_{tot}}$, for the given geometry and "shell"-to-bulk ratio (1st approach).

As a second approach, we can calculate the expected average valence state assuming that the "shell" has a Fe-valence state of 2.67+ (XPS data), whereas the bulk valence state of amosite, determined by Mössbauer spectroscopy, is 2.08+ (Pollastri, 2015). This approach should be

valid, because the XPS data are usually representative of the first 0.3 to 3 nm (Vansant, 1995), and possibly up to 10 nm of the material starting from the surface (Elmi et al., 2016).

Both approaches returned similar results, documenting that the near-surface regions of the short fibers are more oxidized than those of the long fibers (Tab. 2).

Fe–$L_{2,3}$ white-line intensity ratio: standard calibration curves

The calibration curves for the Fe–$L_{2,3}$ white-line intensity ratio were constructed by fitting an exponential function to the $I(L_3)/I(L_2)$ data points obtained from the following standards (Fig. 2): $FeTiO_3$ with all Fe as Fe^{2+} (99.8%, Alfa Aesar, product number 1317), $Co_{0.6}Fe_{2.4}O_4$ with Fe as $Fe^{2.7+}$ (synthesized according to Gyergiek et al., 2010), and Fe_2O_3 with all Fe being Fe^{3+} (99.945%, Alfa Aesar, product number 14680).

The average $L_{2,3}$ ratios and σ_{n-1} values for each standard were determined using multiple analytical points (Fig. 2 and Supplementary S.4). The calibration curve for the standard data points, determined using a 4 eV window (blue dotted line in Fig. 2), shows the smallest $\sigma_{n-1}$with respect to the L_3/L_2 ratio. On the other hand, when the error is calculated for the valence state (horizontal error bar in Fig. 2), the 8 eV window shows the smallest values (excluding the Fe^{2+} data points for which the σ_{n-1} ranges are comparable). The smaller horizontal error bar of the 8 eV calibration curve compared to the 4 eV calibration curve for the $Fe^{2.7+}$ and Fe^{3+} data points is a consequence of the steeper slope of the first one (0.54) compared to the latter one (0.40). The 2 eV calibration curve has the highest slope value (1.27), which limits the error propagation on the valence state, but the large error with respect to the L_3/L_2 ratio generates the largest error on the calculated valence state (Fig. 2 and supplementary figure S.4.1.). In the next section, the valence

state for the studied amosite ROIs will be evaluated using the universal curve and the standard calibration curves determined using a 2 eV, 4 eV, and 8 eV window to confirm the correspondence between the valence state determined using a certain curve and the shape of the $L_{2,3}$ edge and the O–K edge ELNES.

Fe–$L_{2,3}$ white-line intensity ratio: amosite ROIs

The overall average valence states of the investigated ROIs of amosite, obtained by applying the white-line intensity-ratio method to the spectra of short fibers and long fibers, are similar when using the universal curve, the 4 eV window calibration curve or the 8 eV window calibration curve, but the use of a 2 eV window calibration curve returns slightly lower Fe-valence state values (Tab. 3 and supplementary S.5). The σ_{n-1} values are in each case larger for short amosite ROIs than for long amosite ROIs.

The use of the $I(L_3)/I(L_2)$ obtained with 4 eV windows to determine valence state of an ROI, showed a good match with the observed shape and intensity of the L_3 amphibole edges. The application of the universal curve yields a similar overall average valence state to the one obtained by using 4 eV windows on analyses performed on short fibers (Table 3). The long-fiber ROIs have a similar average valence state when using the universal curve, the 4 eV window and the 8 eV window curves.

The valence state for the ROIs of the long fibers are distributed in an area of the chart (Fig. 3) that ranges from 2.10+ to 2.27+, whereas the valence state for the ROIs of the short fibers shows a large variation, ranging from 2.09+ to 3.10+ (Fig. 3). The average valence state for the ROIs of

both long and short fibers is within the bulk valence state (from Mössbauer spectroscopy) and the surface/near-surface valence state (from XPS).

The valence state determined on the amphibole ROIs using the universal curve represents the best match with regard to the intensity and shape of the L_3–edge ELNES and thus, was used for all further evaluations of ELNES spectra (see next section and Discussion).

O–K edge ELNES of amosite

A representative core-loss spectrum (Fig. 4) of an amosite ROI with an Fe-valence state of 2.97+, as assigned through the use of the universal curve (red spectrum in Fig. 4), is characterized by a pre-edge peak, labeled as (a), a dominant peak (b), a weaker maximum at ≈545-550 eV (c) followed by a large bump (d) (not shown), consistent with literature data (Colliex et al., 1991). The pre-edge peak has two main components: one located at 528.25 eV (σ_{n-1}=0.33), the other one at 529.51 eV (σ_{n-1}=0.62). The detected pre-edge is not observed in amosite ROIs with a valence state that is lower than 2.44+, as clearly visible in a representative spectrum from a ROI with a valence state of 2.12+ (green spectrum in Fig. 4). Spectra with a mixed valence state ≥2.44 show variable peak intensity in the O-K pre-edge region (e.g., orange spectrum in Fig. 4).

Fe–$L_{2,3}$ edge ELNES of amosite

The Fe–L_3 and Fe–L_2 edges show features that can be attributed primarily to the oxidation state and, to a lesser extent, to the coordination geometry of Fe in amosite-fiber boundaries (Fig. 5). The L_3 edge is composed of a first peak located at 709.74 (σ_{n-1}=0.14) eV, and a second peak

located at 711.45 (σ_{n-1}=0.15) eV. These two peaks are usually labeled as Fe^{2+} peak and Fe^{3+} peak, respectively since their intensity is characteristic of the related valence state. The L_3 edge of the Fe^{3+}-dominant amosite ROI (red spectrum in Fig. 5) shows a first, less intense shoulder followed by a peak maximum. In the Fe^{2+}-dominant L_3 edge (green line in Fig. 5), the shape of the edge is the inverse, with a more intense first peak, followed by a second, less intense shoulder at higher energy-loss values. The mixed-valence state, assigned using the universal curve, of a representative amosite ROI in between these two extremes (≈2.44+, orange line in Fig. 5) shows an L_3 edge composed of two peaks with similar intensity.

The L_2 edge shows a similar trend, but it tends to be sharper at lower valence states compared to that at higher valence state. The first component of the L_2 edge, representing the more intense peak for Fe^{2+}-dominant ROIs, is located at 722.19 (σ_{n-1}=0.27) eV. The second, less intense component is located at 724.37 (σ_{n-1}=0.18). The intensity maxima are reversed for highly oxidized ROIs (e.g., red spectrum of $Fe^{2.97+}$ in Fig. 5).

The average separation of the L_3- and L_2-edge maxima is 12.54 eV (σ_{n-1}=0.33).

Thickness effect

Since the white-line intensity-ratio method may be influenced by the thickness of the studied ROI, we investigated this possibility by plotting the L_3/L_2-intensity ratio versus thickness (Fig. 6). The plot of the obtained $L_{2,3}$ ratio versus thickness, however, did not reveal any correlation between the two quantities. This diagram further documents a large vertical dispersion of the data points corresponding to a similar thickness.

Discussion

The acSTEM observations show that the amphiboles are far from exhibiting perfect crystal shapes at their grain boundaries. The crystals are in many cases covered by Fe^{3+}-dominated, crystalline or partially amorphized material of variable thickness. The visually observed features are consistent with those observed by ELNES of both the O–K and the Fe–$L_{2,3}$ edges, as well as the associated peaks, and by the valence state, which was determined applying the universal curve. The O–K pre-edge, observed in representative ROIs ($Fe^{2.44+}$ and $Fe^{2.97+}$), is characteristic of ROIs with a valence state equal or greater than 2.44+.

This pre-edge region of the O–K ELNES spectra is worth exploring in more detail: the sharp peak at ≈530eV is related to a high concentration of high-valence 3d transition metals (de Groot et al., 1989). In our experiment, the pre-edge peak was located at 529.51 eV (σ_{n-1}=0.62) and is indicative of Fe^{3+}-rich ROIs, because this peak is visible only in areas with an average valence state ≥2.44+. This peak is assumed to originate from the transition of O–1s core states to O–2p states, which are hybridized with the Fe–3d orbitals (de Groot et al., 1989; Kurata and Colliex, 1993; Garvie 2010). The other pre-edge component, located at ≈528 eV (OH peak), is more controversial. The hypothesis that a 528 eV peak can be directly related to the quantity of OH or H_2O in minerals was refuted by Garvie (2010). The peak we observed in Fe^{3+}-dominant ROIs of amosite at 528.25 eV (σ_{n-1}=0.33) was stable in terms of intensity and did not show the sequence of "appearance" and "disappearance" described in the literature for the so-called OH peak located at ≈528 eV (Garvie, 2010). The observed stability of this peak may be related to several factors, including (i) the relatively low electron dose we applied, estimated at $\approx 1 \cdot 10^3$ electrons/nm^2, and (ii) the peculiar and complex structure at the grain boundaries of the studied fibers. Since we never observed this "OH peak" in the O–K pre-edge region of spectra collected

372 in "shell"-free ROIs, we conclude that it is characteristic of the oxidized "shell" that covers the
373 mineral. This peak may therefore be interpreted as a qualitative indicator of the presence of OH
374 in the "shell" or at the boundary between the "shell" and the real amphibole surface, or as an
375 indicator of a continuous and small loss of hydrogen because of a low electron fluence in
376 scanning mode, which results in a stable intensity of the OH peak. At this level of investigation
377 and conditions, we do agree with Garvie (2010) that it is not possible to use the observed peak
378 for quantification purpose, but this peak could indicate that the Fe^{3+}-rich shell is hydroxylated.
379 On the other hand, we believe that the beam damage, if present, is negligible, since we did not
380 observe a direct increase or decrease in intensity of this peak and the Fe-valence state remained
381 stable. When interrogating the literature for materials that are similar to the investigated shells, a
382 "safe" electron dose that avoids reduction on synthetic 6-line ferrihydrite was determined to be
383 $1 \cdot 10^8$ electrons/nm^2 (Pan et al., 2006), whereas mixed-valent Fe (oxyhydr)oxides (green rust)
384 showed a threshold of $4 \cdot 10^3$ electrons/nm^2 where oxidation begins (Freeman et al., 2019). We
385 thus conclude that at this level of investigation and with our experimental setup, we can
386 reasonably exclude an influence of beam damage on our results.

387 The shape of the Fe^{3+}–L_3 edge is easily recognizable due to the presence of an intense peak at
388 711.45 (σ_{n-1}=0.15) eV and the visibility of a less intense peak (shoulder) at lower energy-loss
389 values (709.74 ± 0.14 eV). On the other hand, the Fe^{2+}-dominant L_3 edges show an opposite
390 trend, with a more intense first peak and a second, less intense shoulder. In the case in which the
391 valence state approaches 2.50+, the two main components of the L_3 edge show similar intensities
392 (Fig. 5). As outlined in the results section, the ELNES shape has an acceptable match with the
393 valence-state values obtained using the calibration curve with a window at 4 eV. Unfortunately,
394 the use of this curve fails when evaluating a valence state that approaches 2.50+. The spectra to

which we assigned an oxidation state of 2.44+ using the universal curve (Fig. 5) has a first intense peak at a lower energy-loss value (709.74 ± 0.14 eV) and a second less intense peak at 711.45 (σ_{n-1}=0.15) eV, which is consistent with the assigned valence state and other spectra of similar minerals in the literature (e.g. ac50hd50 and ac40hd60 pyroxene in Fig. 2b, Van Aken and Liebscher, 2002). In the same spectrum, using the calibration curve with a 4 eV window rather than the universal curve would lead to a valence state of 2.53+. The assigned valence state, thus, would have been in disagreement with the observed ELNES shape since the intensity of the two components of the L_3 peak (located at 709.74 ± 0.14 eV, and 711.45 σ_{n-1}=0.15 eV) indicates a slightly higher amount of Fe^{2+}.

The measured peak separation between the L_3 and L_2 maxima on the amosite ROIs agrees with the work of Van Aken et al. (1998). The peak separations observed in ROIs of fiber boundaries are in the same range, but shifted by ≈0.25 eV to lower electron-loss values. This shift is within the σ_{n-1} range and thus not significant. This small deviation between literature values and experimental results may also be a consequence of symmetry variations or the presence of extra-fine structures (Colliex et al., 1991).

The presence of more distinguishable features occurring in the Fe^{2+}–L_2 edges can be related to six-fold coordination. In more oxidized ROIs, the L_2 edges have poor features, a condition that can be related to a coordination geometry of 6 (structural Fe^{3+}) or lower, which may correspond to the presence of amorphous material or surface-bonded Fe^{3+} (Van Aken and Liebscher, 2002). In addition to valence state and coordination geometry, there is a possibility that the presence of Al^{3+} can shape the ELNES, leading to an increase in the intensity of the right flank of the Fe–L_3 edge located at 711.45 (σ_{n-1}=0.15) eV, thus affecting the results of the white-line intensity-ratio calculation (Frost and Langenhorst, 2002; Langenhorst et al., 2013). In our case, we believe that

418 the influence of Al_2O_3 is minimal, if not negligible, since the Al_2O_3 concentration determined by
419 wavelength-dispersive X-ray spectroscopy is only 0.04 wt % (Pollastri et al., 2014).

420 The use of a different size and position of the integration window when applying the Fe–$L_{2,3}$
421 white-line intensity-ratio method for the study of different compounds may affect the results
422 depending on small differences in the ELNES shape (Tan et al., 2012). This effect may be larger
423 for a narrow window, and could be influenced by both the ELNES shape and the spectral noise.
424 The use of wider windows for the definition of the calibration curve through the standards
425 resulted in a reduced σ_{n-1} for the windows at 4 eV and 8 eV for each of the valence states (2+,
426 2.7+, and 3+) of the standards, and thus a better fit of the calibration curve. The data series
427 obtained with the 4 eV window showed slightly lower σ_{n-1} values, but a poor qualitative
428 correspondence to the spectral ELNES. The use of the universal curve returned a better
429 correspondence among the measured valence state and the ELNES shape. Despite the similarity
430 of average results obtained using the universal curve and the calibration curves derived from our
431 standards (with the 4 eV and 8 eV windows), in this specific case the use of a larger window (8
432 eV) probably yields less good results because of the possible presence of additional structures in
433 the low- and high-end tails of the considered edges generated by the influence of multiplet
434 splitting and crystal-field effects (Van Aken et al., 1998).

435 Our experiment did not provide any evidence for a correlation between $L_{2,3}$ ratios and the sample
436 thickness (Fig. 6), consistent with the results of other studies (Wang et al., 2000; Schmid and
437 Mader, 2006; Loomer et al., 2007; Varela et al., 2009). However, we think that moving to higher
438 magnification and approaching an atomic scale investigation, the thickness may considerably
439 influence the results when applying the white-line intensity ratio, as noted by Tan et al. (2012).
440 The experimentally calculated average valence state on the surface of amosite fibers using XPS

441 ($Fe^{2.67+}$) is considerably higher than the one reported for the bulk of the same sample ($Fe^{2.08+}$)
442 (Pollastri et al., 2015). This discrepancy between the bulk and the surface, however, is not
443 unusual, since surfaces are typically more oxidized than the bulk (Fantauzzi et al., 2010).
444 Moreover, it reflects the presence of a hydrated Fe^{3+}-dominant "shell", which we observed in
445 acSTEM images.

446 Our Dual-EELS results revealed an average valence state of 2.44+ (σ_{n-1}=0.31) and 2.19+ (σ_{n-}
447 $_1$=0.05) for the studied ROIs in the short and long fibers, respectively, when using the universal
448 curve. These results (Fig. 3) are within the range defined by the bulk amosite analysis ($Fe^{2.08+}$;
449 Pollastri et al., 2015) and the data obtained by XPS for the surface and near-surface layers of
450 amosite ($Fe^{2.67+}$, Table 1). Short fibers, characterized by a larger surface area (≈9.5 m^2/g;
451 Pollastri et al., 2014), are more likely to be heterogeneously covered by an oxidized "shell",
452 consistent with our observations and the larger range of valence states that we have recorded
453 (Fig. 3 and supplementary S.5.1.). Long fibers, however, have a smaller surface area (≈3.9 m^2/g;
454 Pollastri et al., 2014), and a thinner or less extended "shell", resulting in a lower average valence
455 state and σ_{n-1} (Fig. 3 and supplementary S.5.2.), which is a consequence of the major
456 contribution of the nearly completely reduced bulk amosite. The Dual-EELS investigation allows
457 a researcher to effectively relate visual observations to the valence state of a certain ROI, thus
458 enabling a better description of the crystallochemical state and transformation of a fiber
459 boundary compared to that derived from XPS data.

460 The use of Mössbauer spectroscopy and XPS is fundamental and faster when the valence state of
461 an entire fiber population needs to be estimated. On the other hand, Dual-EELS provides unique
462 information on the high heterogeneity of the valence state, geometry and amorphous shell

463 coverage of the ROIs, and further allows for visualization of the crystal structure and boundaries
464 of the analyzed crystals.

465 We have shown a good correspondence between the valence state estimated through our
466 geometrical model and the valence state obtained through Dual-EELS and the associated
467 statistical errors ($\pm\sigma_{n-1}$): for short fibers, the valence state calculated from geometric
468 considerations (1st approach) was 2.49+ (σ_{n-1}=0.44), i.e. similar to the real valence state of 2.44
469 (σ_{n-1}=0.31), as determined by Dual-EELS (universal curve). For long fibers, the valence state
470 calculated from geometric considerations was 2.21+ (σ_{n-1}=0.10), again very similar to the one
471 determined experimentally (universal curve), which was equal to 2.19+ (σ_{n-1}=0.05). As observed
472 for the experimental values, the standard deviation calculated from the theoretical model for the
473 ROIs of short amosite fibers is larger than the one for the ROIs of long amosite fibers (Tab. 2
474 and 3).

475 The 2nd geometric approach resulted in a valence state of 2.35+ for short fibers and 2.15+ for
476 long fibers, both lower than the values obtained by the 1st approach and experimentally. Whereas
477 the long-fiber valence state is similar for the experimental results and the geometry-based
478 calculation (Difference of 0.04), there is a difference of 0.09 between the experimental valence
479 state and the calculated valence state in short fibers when using the 2nd geometric approach. This
480 discrepancy may be a consequence of the unknown depth of analysis of the XPS starting from
481 the surface, causing the impossibility to know the "shell" versus bulk ratio using this approach.

482

483 **Implications**

The use of acSTEM Dual-EELS on amosite asbestos fibers represents a powerful tool, which allows for relating the morphometry, crystallochemistry, and valence state of a specific investigated area. The use of different integration-window widths and positioning may be dependent on the analyzed material, standards, and instrument, and thus it is important to test the universal curve versus different calibration curves and verify their correspondence to the observed ELNES shape. In this comparison, the coordination geometry and elements that may affect the ELNES shape (e.g., Al^{3+}) should be considered. We demonstrated that the Dual-EELS results for amosite boundaries are in good agreement with the valence-state estimates obtained using a simplified geometrical model, which was derived by combining the visual information acquired by acSTEM and the determination of the bulk (Mössbauer spectroscopy) and surface/near-surface (XPS) valence-state.

The determination of the Fe-valence state at the surface of mineral fibers is of pivotal importance since Fe may act as electron donor in ROS generation within biological systems. Surface-bonded Fe^{2+} has been shown to react faster with molecular oxygen than dissolved Fe (Schoonen et al., 2006). This higher reaction speed can play a major role in disrupting the redox state of biological materials (e.g., cells, tissues, and biofluids). This mechanism, therefore, needs to be explored in greater detail, leading to a step-by-step description at the higher available spatial resolution, since surfaces are highly heterogeneous with respect to their topography, physical state (e.g., zeta potential) and chemical composition. This surface heterogeneity is poorly depicted using methods, such as XPS, but acSTEM Dual-EELS can provide fundamental information in this regard, which will help in understanding the overall processes that take place at the boundary between a mineral and its surrounding environment.

Acknowledgments

This research was supported by a Rotary Global Grant (GG1640842) awarded to Dr. Ruggero Vigliaturo and grant P2-0393 from Slovenian Research Agency. The study was further supported in part by grants P30-ES013508 and P42-ES023720 awarded by the National Institute of Environmental Health Sciences (NIEHS). The findings are not the official opinions of NIEHS or NIH. The XPS spectra were kindly collected by Th. Dikonimos Makris (ENEA, Casaccia Research Center, Materials and New Technologies Unit, Rome, Italy).

We sincerely thank the two anonymous reviewers whose fundamental comments, suggestions and critical reading helped us in improving and clarifying this manuscript.

References

Andreozzi G.B., Pollastri S. (2017). Bulk spectroscopy of mineral fibres. EMU notes in Mineralogy, Vol. 18, Chapter 4, 111-134

Cavé L., Al T., Loomer D., Cogswell S., Weaver L. (2006). A STEM/EELS method for mapping iron valence ratios in oxide minerals. Micron 37, 301–309

Colliex C., Manoubi T., Ortiz C. (1991). Electron-energy-loss-spectroscopy near-edge fine structures in the iron-oxygen system. Physical Review B, 44(20), 11402-11411

de Groot, F.M.F., Grioni, M., Fuggle, J.C., Ghijsen, J., Sawatzky, G.A., and Petersen, H. (1989) Oxygen 1s X-ray-absorption edges of transition-metal oxides. Physical Review B, 40, 5715–5723

527 Droop G.T.R. (1987). A General Equation for Estimating Fe3+ Concentrations in
528 Ferromagnesian Silicates and Oxides from Microprobe Analyses, Using Stoichiometric Criteria.
529 Mineralogical Magazine, 51(361), 431-435

530 Elmi C., Guggenheim S., Gieré R. (2016). Surface crystal chemistry of phyllosilicates using X-
531 Ray photoelectron spectroscopy: A review. Clays and Clay Minerals, 64(5), 537-551.

532 Fantauzzi M., Pacella A., Atzei D., Gianfagna A., Andreozzi G.B., Rossi A. (2010). Combined
533 use of X-ray photoelectron and Mössbauer spectroscopic techniques in the analytical
534 characterization of iron oxidation state in amphibole asbestos. Anal Bioanal Chem 396: 2889

535 Ferro A., Zebedeo C.N., Davis C., Ng K.W., and Pfau J.C. (2013). Amphibole, but not
536 chrysotile, asbestos induces antinuclear autoantibodies and IL-17 in C57BL/6 mice. Journal of
537 Immunotoxicology, 11(3):283-90

538 Freeman H.M., Perez J.P.H., Hondow N., Benning L.G., and A.P. Brown. (2019). Beam-induced
539 oxidation of mixed-valent Fe (oxyhydr)oxides (green rust) monitored by STEM-EELS. Micron
540 (In press), https://doi.org/10.1016/j.micron.2019.02.002

541 Frost D., Langenhorst F. (2002). The effect of Al_2O_3 on Fe-Mg partitioning between
542 magnesiowüstite and magnesium silicate perovskite. Earth and Planetary Science Letters, 199,
543 227-241.

544 Garvie L.A.J., Buseck P.R. (1998). Ratios of ferrous to ferric iron from nanometre-sized areas in
545 minerals. Nature volume 396, 667–67

546 Garvie L.A.J. (2010). Can electron energy-loss spectroscopy (EELS) be used to quantify
547 hydrogen in minerals from the O K edge? American Mineralogist 95, 92-97

548 Graetz J., Ahn C. C., Ouyang H., Rez P., Fultz B. (2004). White lines and d-band occupancy for
549 the 3d transition-metal oxides and lithium transition-metal oxides. Phys. Rev. B 69, 235103

550 Gualtieri A.F., Bursi-Gandolfi N., Pollastri S., Pollok K., Langenhorst F. (2016). Where is iron in
551 erionite? A multidisciplinary study on fibrous erionite-Na from Jersey (Nevada, USA). Scientific
552 Reports **6**, 37981

553 Gyergyek S., Makovec D., Kodre A., Arčon I., Jagodič M., Drofenik M. (2010). Influence of
554 synthesis method on structural and magnetic properties of cobalt ferrite nanoparticles. J.
555 Nanopart. Res. 12, 263–1273

556 Iakoubovskii K., Mitsuishi K., Nakayama Y., Furuya K. (2008). Thickness measurements with
557 electron energy loss spectroscopy. Microsc Res Tech. 71(8):626-31

558 Jablonski R.P., Kim S.J., Cheresh P., Liu G., Kamp D.W. (2017). Insights into mineral fibre-
559 induced lung epithelial cell toxicity and pulmonary fibrosis. EMU Notes in Mineralogy, Vol. 18 ,
560 Chapter 14, 447-500

561 Kurata, H. and Colliex, C. (1993) Electron-energy-loss core-edge structures in manganese
562 oxides. Physical Review B 48, 2102–2108

563 Langenhorst F., Harries D., Pollok K. (2013). Non-stoichiometry, defects and superstructures in
564 sulfide and oxide minerals. EMU Notes in Mineralogy, Vol. 14, Chapter 8, 261-295

565 Leapman R. D., Grunes L. A. (1980). Anomalous L3/L2 white-line ratios in the 3d transition
566 metals Phys. Rev. Lett. 45, 397

567 Lee J.A., Newnham C.E., Stone F.S., Tye F.l. (1980), Journal of Solid State Chemistry 31(1), 81-
568 93

569 Li M., Gunter M.E., Fukagawa N.K. (2012). Differential activation of the inflammasome in
570 THP-1 cells exposed to chrysotile asbestos and Libby, "six-mix" amphiboles and subsequent
571 activation of BEAS-2B cells. Cytokine, vol. 60, no. 3, 718–730

572 Loomer D.B., Al T.A., Weaver L., Cogswell S. (2007). Manganese valence imaging in Mn
573 minerals at the nanoscale using STEM-EELS. American Mineralogist, 92, 72–79

574 Malis T., Cheng S.C., Egerton R.F. (1988) EELS log ratio technique for specimen-thickness
575 measurement in the TEM. J. Electron Microscope Technique. 8:193

576 Mitchell D.R.G. (2015). Double_Atan_EELS_Background.s Digital Micrograph Script, version :
577 20150402, v2.0, www.dmscripting .com

578 Pacella A., Andreozzi G.B., Fournier J., Stievano L., Giantomassi F., Lucarini G., Rippo M.R.,
579 Pugnaloni A. (2012). Iron topochemistry and surface reactivity of amphibole asbestos: relations
580 with in vitro toxicity. Anal Bioanal Chem 402:871–881

581 Pacella A., Fantauzzi M., Turci F., Cremisini C., Montereali M.R., Nardi E., Atzei D., Rossi A.,
582 Andreozzi G.B. (2015). Surface alteration mechanism and topochemistry of iron in tremolite
583 asbestos: A step toward understanding the potential hazard of amphibole asbestos. Chemical
584 Geology 405, 28–38

585 Pan Y., Brown A., Brydson R., Warley A., Li A., Powell J. (2006). Electron beam damage
586 studies of synthetic 6-line ferrihydrite and ferritin molecule cores within a human liver biopsy.
587 Micron 37, 403-411

588 Pfau J.C., Serve K.M., Noonan C. (2014). Autoimmunity and Asbestos Exposure. Autoimmune
589 Diseases, vol. 2014, Article ID 782045, 11 pages

590 Pollastri S., Gualtieri A.F., Gualtieri M.L., Hanuskova M., Cavallo A., Gaudino G. (2014). The
591 zeta potential of mineral fibres. Journal of Hazardous Materials 276 469–479

592 Pollastri S., D'Acapito F., Trapananti A., Colantonic I., Andreozzi G.B., Gualtieri A.F. (2015).
593 The chemical environment of iron in mineral fibres. A combined X-ray absorption and
594 Mössbauer spectroscopic study. Journal of Hazardous Materials 298, 282–293

595 Potapov P.L., Schryvers D. (2004). Measuring the absolute position of EELS ionisation edges in
596 a TEM. Ultramicroscopy 99, 73-85

597 Riedl T., Gemming T., Gruner W., Acker J., Wetzig K. (2007). Determination of manganese
598 valency in $La_{1-x}Sr_xMnO_3$ using ELNES in the (S)TEM. Micron 38, (3)24-230

599 Rojac T., Bencan A., Drazic G., Sakamoto N., Ursic H., Jancar B., Tavcar G., Makarovic M.,
600 Walker J., Malic B., Damjanovic D. (2017). Domain-wall conduction in ferroelectric BiFeO3
601 controlled by accumulation of charged defects. Nature Materials 16, 322–327

602 Schmid H.K., Mader W. (2006). Oxidation states of Mn and Fe in various compound oxide
603 systems. Micron 37, 426–432

604 Schoonen M.A.A., Cohn C.A., Roemer E., Laffers R., Simon S.R., O'Riordan T. (2006).
605 Mineral-induced formation of reactive oxygen species. In: Sahai N., Schoonen M.A.A. (eds).
606 Medical Mineralogy and Geochemistry. Rev Mineral Geochem 64: 179-221

607 Sparrow, T., Williams, B., Rao, C., Thomas, J. (1984). L3/L2 white-line intensity ratios in the
608 electron energy-loss spectra of 3d-transition metal oxides. Chem. Phys. Lett. 108, 547–550

609 Taftø J., Krivanek O.L. (1982). Site-Specific valence determination by Electron Energy-Loss
610 Spectroscopy. Phys. Rev. Lett. 48, 560

Tan H., Verbeeck J., Abakumov A., VanTendeloo G. (2012). Oxidation state and chemical shift investigation in transition metal oxides by EELS. Ultramicroscopy 116, 24–33.

Thole B.J., Van der Laan, G. (1988). Branching ratio in X-ray absorption spectroscopy. Phys. Rev. B 38, 3158–3171

Van Aken P.A., Liebscher B., Styrsa V.J. (1998). Quantitative determination of iron oxidation states in minerals using Fe L2,3-edge electron energy-loss near-edge structure spectroscopy. Phys Chem Minerals 25, 323-327

Van Aken P.A., Liebscher B. (2002). Quantification of ferrous/ferric ratios in minerals: new evaluation schemes of Fe L_{23} electron energy-loss near-edge spectra. Physics and Chemistry of Minerals 29(3), 188–200

Ed. Vansant E.F., Van Der Voort P., Vrancken K.C. (1995). Appendix B XPS X-ray photoelectron spectroscopy, Studies in Surface Science and Catalysis, Elsevier, 93, 501-504

Varela M., Oxley M. P., Luo W., Tao J., Watanabe M., Lupini A. R., Pantelides S. T., Pennycook S. J. (2009). Atomic-resolution imaging of oxidation states in manganites. Physical Review B 79, 085117

Wang Z. L., Yin J. S., Jiang Y. D. (2000). EELS analysis of cation valence states and oxygen vacancies in magnetic oxides. Micron 31, 571

632 **Figure captions**

633 **Fig. 1**

634 a) Micrograph collected in acSTEM bright-field mode showing an oriented amphibole-fiber boundary covered by an
635 irregular amorphous "shell". The ROI width is parallel to [010], whereas the ROI length runs parallel to the c* axis
636 of the fiber. b) Geometric reconstruction of a fiber boundary oriented with respect to the electron beam. The green
637 area is the amphibole bulk (Fe^{2+} dominant), whereas the red area is the "shell" (Fe^{3+} dominant). Both ROI length and
638 ROI width are 25 nm long. The image proportions correspond to a long fiber.

639

640 **Fig. 2**

641 Calibration curves defined by the three standards using different integration-window widths. The universal curve
642 (from Van Aken et al., 1998) is shown for reference (black continuous line). The red dashed line was determined by
643 using a 2 eV integration window (fit to the data points shown as red dots), the blue dotted line was determined by
644 using a 4 eV window (fit to the data shown as blue squares), and the green dash-dotted line was determined by using
645 a 8 eV window (fit to the data shown as green triangles). Error bars are σ_{n-1}.

646

647 **Fig. 3**

648 The green dashed vertical line (M.s.) represents the bulk valence state (Mössbauer spectroscopy – Pollastri, 2015).
649 The red dashed vertical line represents the near-surface valence state (XPS). The universal curve (dashed grey
650 curve) together with the $\Delta(Fe^{3+}/\Sigma Fe)$ error range equal to ± 0.03 (grey dotted curves)(Van Aken, 2002) is shown for
651 reference. The black crosses represent L_3/L_2 ratio and valence state for ROIs of the short fibers, whereas the yellow
652 crosses represent the same data for ROIs of the long fibers. The blue squares and error bars (σ_{n-1}) show the average
653 L_3/L_2 ratio and valence state for the ROIs of short fibers and long fibers . The yellow dashed vertical line represents
654 the valence state obtained by the 1st geometrical model for long fibers (G.l.a.), whereas the orange dashed vertical
655 line shows the valence state of the short fibers (G.s.a.).

656

Fig. 4

Selected O–K edges corresponding to representative amosite ROIs for $Fe^{2.12+}$ (green), $Fe^{2.44+}$ (orange), and $Fe^{2.97+}$ (red). Valence states were assigned by using the universal curve. For clarity, feature labels are shown only in the $Fe^{2.97+}$ spectrum.

Fig. 5

Selected Fe–$L_{2,3}$ edges (before arctangent background removal) corresponding to representative ROIs in amosite with valence states of 2.12+ (green), 2.44+ (orange), and 2.97+ (red), respectively. Valence states were assigned by using the universal curve. For clarity, $L_{2,3}$ edge labels are shown only in the $Fe^{2.97+}$ spectrum.

Fig. 6

Relationship between the white-line intensity ratio and the thickness in different amosite ROIs (n = 66). Each ROI is represented by a square, the dotted line is the linear fit to the data points.

This is a preprint, the final version is subject to change, of the American Mineralogist (MSA)
Cite as Authors (Year) Title. American Mineralogist, in press.
DOI: https://doi.org/10.2138/am-2019-7218

XPS analysis

Sample	$Fe(II)/Fe_{tot}$	$Fe(III)/Fe_{tot}$	$FeOOH/Fe_{tot}$
Amosite	33 (3)	26 (4)	41 (4)

Table 1: Concentration of Fe^{2+}, Fe^{3+} and FeOOH, as determined by XPS, compared to the total iron present in the analyzed region. The standard deviation (σ_{n-1}) is given in parentheses.

This is a preprint, the final version is subject to change, of the American Mineralogist (MSA)
Cite as Authors (Year) Title. American Mineralogist, in press.
DOI: https://doi.org/10.2138/am-2019-7218

Geometrical model parameters and estimated valence state.

	Width of ROI ($h_{trapezoid}$)	Thickness of ROI ($\frac{B+b}{2}$)	Average "Shell" thickness	Fe-valence state 1st approach	Fe-valence state 2nd approach
Short fibers	25 nm	16.25(7.69) nm	3.74(2.30) nm	2.49(0.44)	2.35(0.48)
Long fibers		25.30(9.77) nm	1.99(0.88) nm	2.21(0.10)	2.15(0.14)

Table 2

Summary of all geometric parameters used to estimate the valence state of amosite ROIs using two different approaches. All values in parentheses are σ_{n-1}.

This is a preprint, the final version is subject to change, of the American Mineralogist (MSA)
Cite as Authors (Year) Title. American Mineralogist, in press.
DOI: https://doi.org/10.2138/am-2019-7218

ROI characteristics summary

			Valence state							
				White-line intensity ratio (Windows)			Geometrical model		(Pollastri, 2015)	
		ROI thickness (nm)	Universal curve (2eV)	2 eV	4 eV	8 eV	1st	2nd	Bulk (Mössbauer)	XPS
Short amosite	Mean	16.25	2.44	2.33	2.47	2.57	2.49	2.35	2.08	2.67 (4)
	σ_{n-1}	7.69	0.31	0.38	0.31	0.25	0.44	0.48		
Long amosite	Mean	25.30	2.19	2.01	2.16	2.17	2.21	2.15		
	σ_{n-1}	9.77	0.05	0.07	0.19	0.20	0.10	0.14		

Tab. 3

Valence states obtained using progressively larger integrating windows for short and long amosite fibers. For the XPS measurement, the standard deviation (σ_{n-1}) is given in parenthesis.

This is a preprint, the final version is subject to change, of the American Mineralogist (MSA)
Cite as Authors (Year) Title. American Mineralogist, in press.
DOI: https://doi.org/10.2138/am-2019-7218

Figure 1

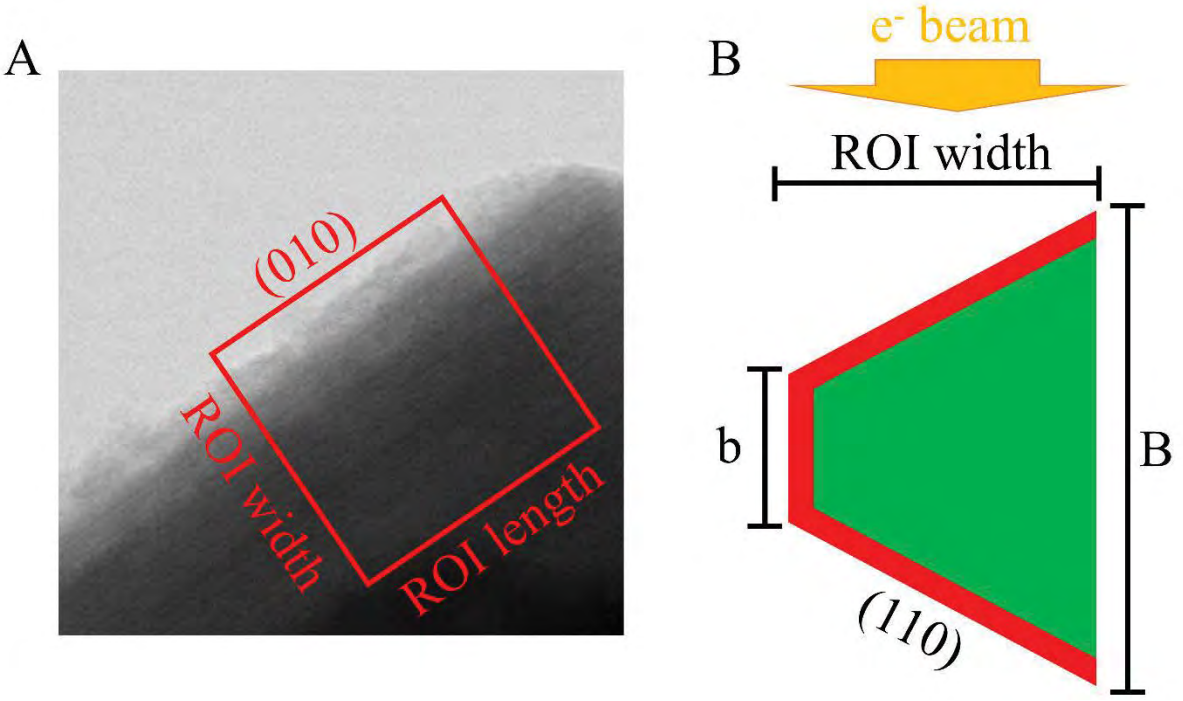

This is a preprint, the final version is subject to change, of the American Mineralogist (MSA)
Cite as Authors (Year) Title. American Mineralogist, in press.
DOI: https://doi.org/10.2138/am-2019-7218

Figure 2

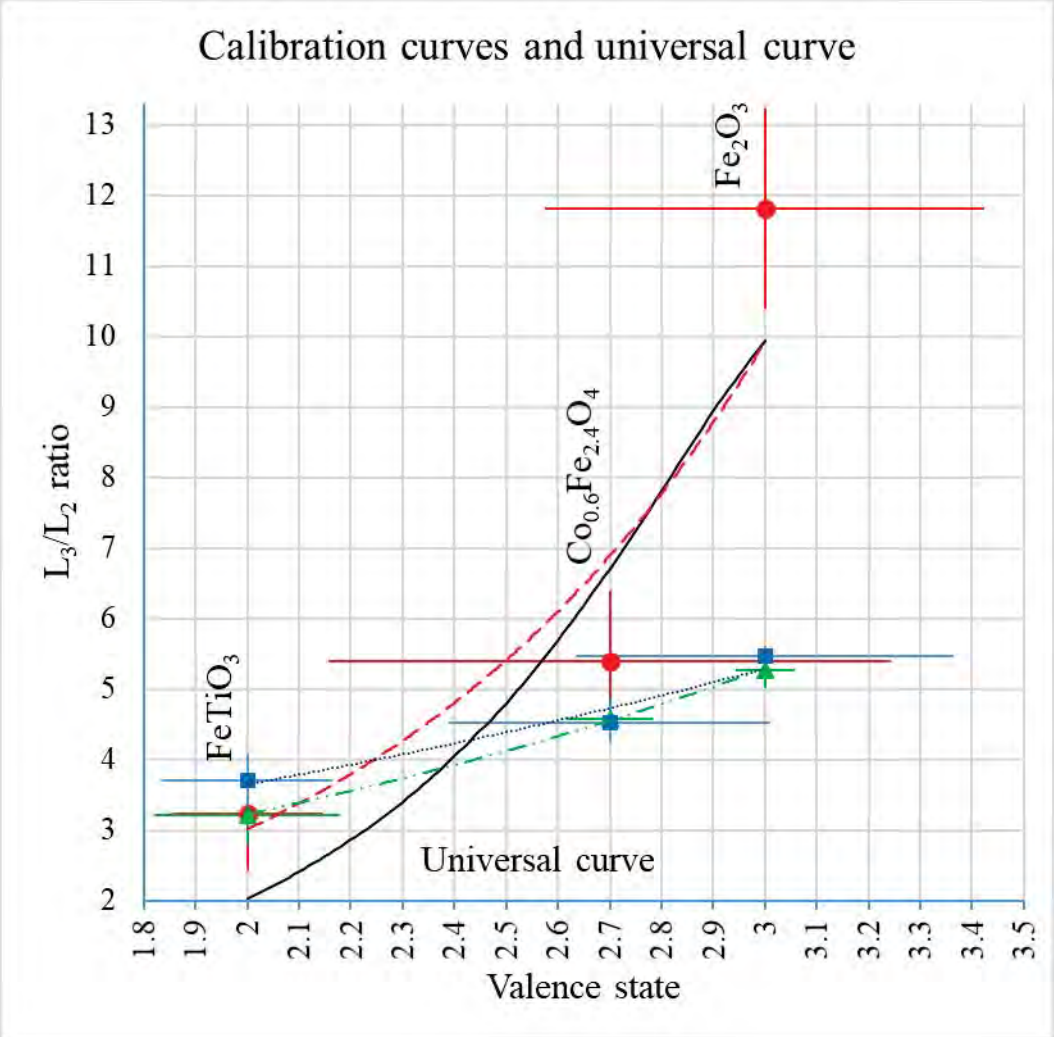

This is a preprint, the final version is subject to change, of the American Mineralogist (MSA)
Cite as Authors (Year) Title. American Mineralogist, in press.
DOI: https://doi.org/10.2138/am-2019-7218

Figure 3

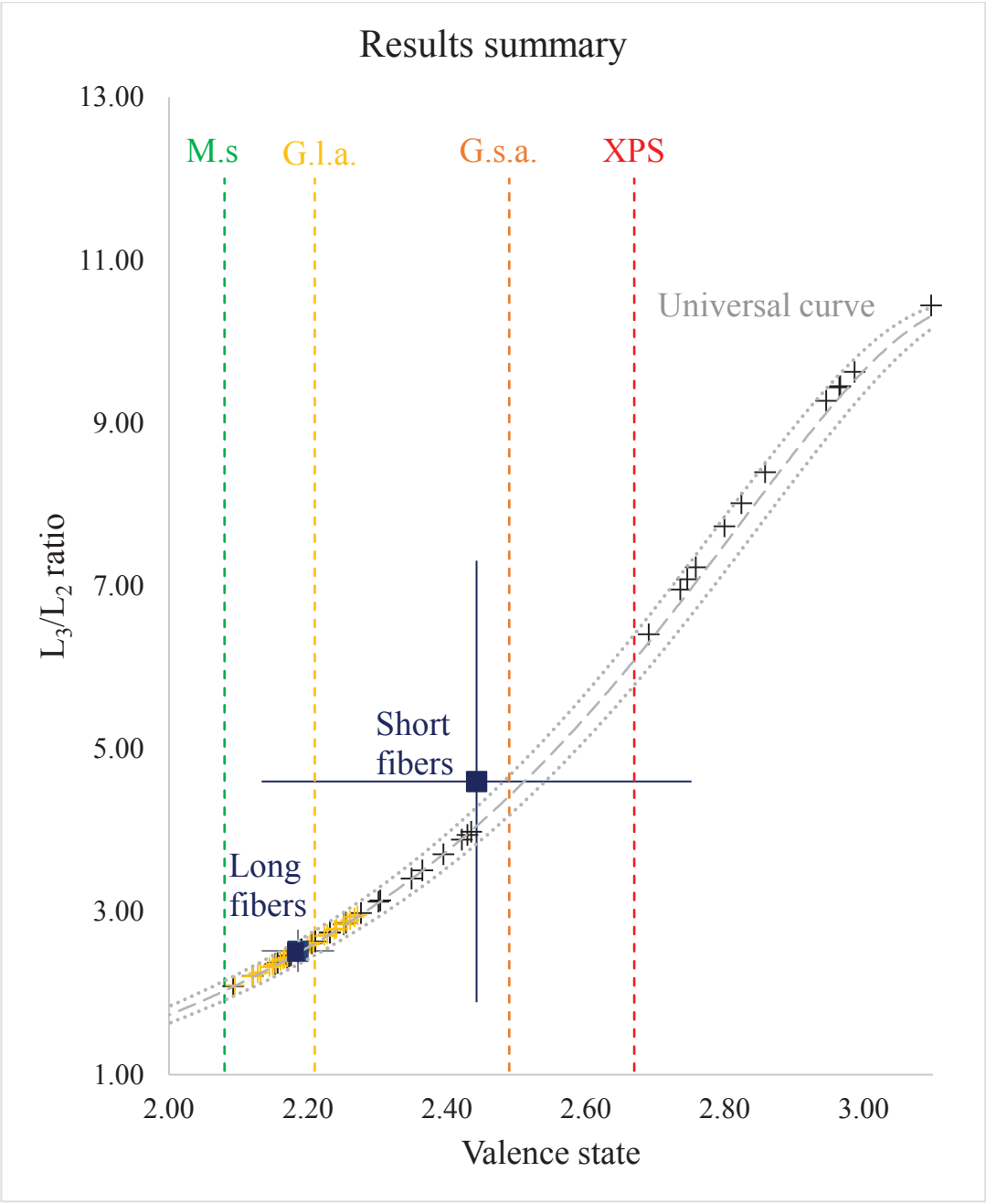

This is a preprint, the final version is subject to change, of the American Mineralogist (MSA)
Cite as Authors (Year) Title. American Mineralogist, in press.
DOI: https://doi.org/10.2138/am-2019-7218

Figure 4

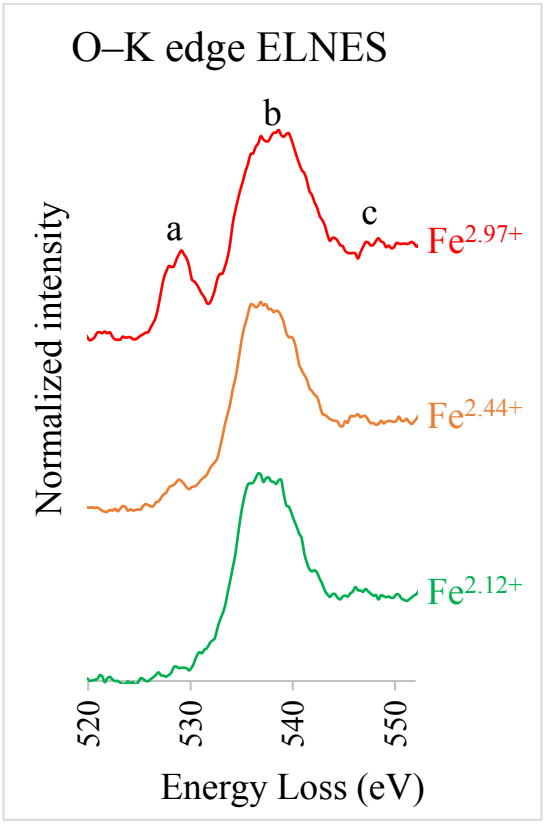

This is a preprint, the final version is subject to change, of the American Mineralogist (MSA)
Cite as Authors (Year) Title. American Mineralogist, in press.
DOI: https://doi.org/10.2138/am-2019-7218

Figure 5

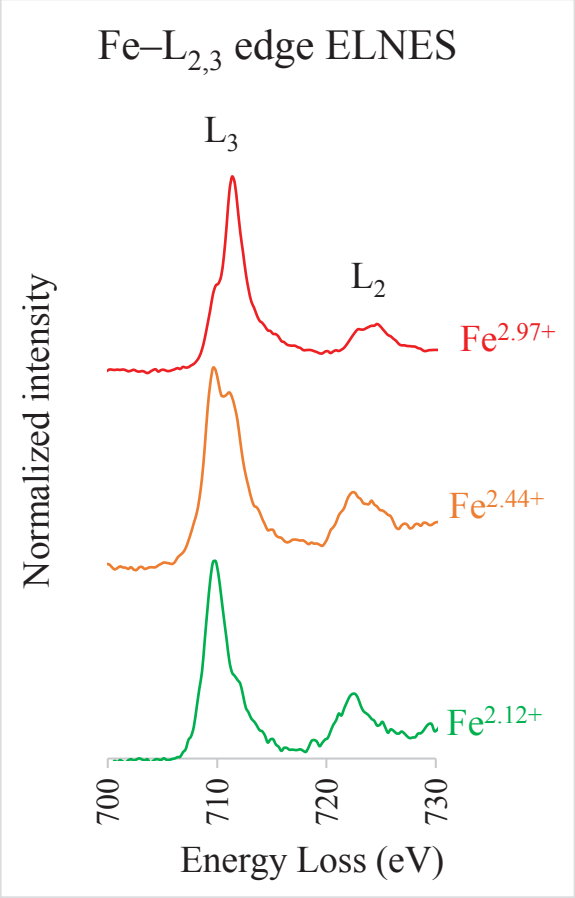

This is a preprint, the final version is subject to change, of the American Mineralogist (MSA)
Cite as Authors (Year) Title. American Mineralogist, in press.
DOI: https://doi.org/10.2138/am-2019-7218

Figure 6